RSC Advances

PAPER

View Article Online
View Journal | View Issue

Cite this: *RSC Adv.*, 2019, **9**, 15917

The effects of additions of two-dimensional graphitic-C_3N_4 on the negative electro-caloric effects in P(VDF-TrFE) copolymers

Sana Ullah,[a] Hao Wang,[b] Bin Liu, [c] Junye Cheng, *[c] Guangcun Shan *[d] and Guang-Ping Zheng *[a]

In order to enhance and tune the electrocaloric effect (ECE) and ferroelectric responses, nanocomposites containing ferroelectric copolymer poly(vinylidene fluoride trifluoroethylene) and two-dimensional (2D) graphitic-C_3N_4 (g-C_3N_4) are synthesized. The effects of g-C_3N_4 on the ferroelectric-to-paraelectric phase transition of the copolymer are investigated by the differential scanning calorimetry (DSC), P–E hysteresis loop and dielectric spectrum measurements. The results indicate that the addition of 2D g-C_3N_4 in the ferroelectric copolymer is an effective approach in enhancing its dielectric and ferroelectric properties. Furthermore, the nanocomposites show the maximum absolute value of negative electrocaloric effect (ECE) of 5.4 K at 322 K under an electric field of 0.45 MV cm^{-1}, which is much better than that of pristine copolymer. The negative ECE of the nanocomposites can be well explained by the Kauzmann theory. The low cost and enhanced negative ferroelectric properties of P(VDF-TrFE) make them more feasible over ceramics materials such as lead zirconate titanate (PZT) based ferroelectrics for applications in electrocaloric refrigeration.

Received 31st March 2019
Accepted 7th May 2019

DOI: 10.1039/c9ra02428j

rsc.li/rsc-advances

1. Introduction

Polyvinylidene fluoride (PVDF) and copolymer poly(vinylidene fluoride trifluoroethylene), *i.e.*, P(VDF-TrFE), have attracted great attention due to their ferroelectric, pyroelectric and piezoelectric properties.[1] The piezo-, pyro- and ferro-electric properties of PVDF and P(VDF-TrFE) lead to their outstanding technological applications in infrared detection,[2,3] sensor and actuators,[4,5] and infrared imaging,[2,6,7] while their flexibility, convenience in processing and ferroelectric properties make them more feasible over ceramics materials such as lead zirconate titanate (PZT) based ferroelectrics for practical applications. PVDF shows α, β, γ or δ crystalline phases depending on processing conditions.[7–9] The polar β-phase is of technological importance due to its ferroelectric properties. The β-phase of PVDF can be achieved by annealing or by mechanical stretching and electrical poling.[10] In the P(VDF-TrFE) copolymer the crystal defects in the PVDF can be reduced by the addition of fluorine atoms, leading to the increased crystallinity of the copolymer.[11] The copolymer P(VDF-TrFE) can crystallize with the same chain conformation as the β-PVDF,[12] if the content of TrFE is more than 18%. The ferroelectric properties of P(VDF-TrFE) is much better than those of PVDF due to the existence of intrinsic β-phase in P(VDF-TrFE).[12]

Electrocaloric effect (ECE) is the adiabatic temperature change or in another terms it is the change in the isothermal entropy of the dielectric material with the support of an application or withdrawal of an electric field, which is first study in 1930.[13] In conventional ferroelectrics the net polarization increases with the application of an electric field or decreases with increasing working temperature, leading to the conventional ECE; whereas recently some ferroelectric ceramics and nanocomposites are found to exhibit a negative ECE. Due to the negative ECE, the dipolar disorder increases and causes the ferroelectric material to absorb more heat by the application of an external electric field,[14,15] also manifesting itself by the increased polarization with increasing temperature. Combined with conventional ECE, the negative ECE provides with us viable routes to implement EC refrigeration, which is much desirable for energy-efficient, environmental-friendly and solid-state refrigeration especially in the cooling of microelectronics. However, the strength of negative ECE is much smaller than that of conventional ECE. Taking P(VDF-TrFE) thick films as examples, the strength of negative ECE is less than 2.0 °C (MV cm^{-1})$^{-1}$, while that of conventional ECE can be as high as 15 °C (MV cm^{-1})$^{-1}$.

[a]*Department of Mechanical Engineering, The Hong Kong Polytechnic University, Hung Hom, Kowloon, Hong Kong, China. E-mail: mmzheng@polyu.edu.hk*

[b]*Guangdong Provincial Key Laboratory of Micro/Nano Optomechatronics Engineering, College of Mechatronics and Control Engineering, Shenzhen University, Shenzhen 518060, China*

[c]*Center of Super-Diamond and Advanced Films, Department of Materials Science and Engineering, City University of Hong Kong, Hong Kong 999077, China. E-mail: jycheng4-c@my.cityu.edu.hk*

[d]*School of Instrument Science and Opto-electronics Engineering, Beihang University, No. 37 XueYuan Road, Beijing 100083, China. E-mail: gcshan@buaa.edu.cn*

Through the introduction of nano-fillers into the copolymer matrix,[16,17] the ferroelectric and piezoelectric properties of the resulting nanocomposites are dramatically enhanced. The nano-filler in the matrix enhanced the piezoelectric, ferroelectric and mechanical properties of the nanocomposite as compared with those of the host materials.[18,19] The enhanced ferroelectric properties of P(VDF-TrFE)-based nanocomposite offer many advantages. For examples, huge conventional ECE at room temperature is reported for the nanocomposites.[20,21] High dielectric constants of the nanocomposites result in high breakdown strength.[22] The additions of ceramic nano-fillers into the P(VDF-TrFE) matrix are reported to exhibit ultra-high energy density for electrical energy storage.[23–25] Nonetheless, there is few report on enhancing the negative ECE in P(VDF-TrFE)-based nanocomposites.

In this work, two-dimensional (2D) graphitic-C_3N_4 (g-C_3N_4) nano-fillers are introduced into P(VDF-TrFE) copolymer to improve its dielectric and ferroelectric properties. To the best of our knowledge, it is the first time that 2D g-C_3N_4 are used as nano-fillers in the P(VDF-TrFE)-based nanocomposites. The nanocomposites with various contents of g-C_3N_4 are characterized by different techniques such as FTIR, XRD, PFM and SEM, and the differential scanning calorimetry (DSC) is employed to explore the effects of g-C_3N_4 on the ferroelectric-to-paraelectric (FE-to-PE) phase transition and the kinetics of crystallization process in the nanocomposites. The enhanced dielectric and negative electrocaloric effects of the nanocomposites are investigated, and the effects of 2D g-C_3N_4 on those properties are discussed. More importantly, the mechanisms of negative ECE in the nanocomposites are elucidated from the experimental results.

2. Experimental methods

The g-C_3N_4 powders were prepared by the calcination of melamine in a muffle furnace at 600 °C in air. The powders were then mixed with HNO_3 and deionized water and were sonicated to form suspensions. The mixture solution was centrifuged to form g-C_3N_4 nanosheets, which were finally washed and dried to obtain g-C_3N_4 nano-powders. The nanocomposites containing P(VDF-TrFE) and g-C_3N_4 were prepared by adding 0.3 grams of copolymer [P(VDF-TrFE)-52/48 mol%, Piezotech, France] into the 5 grams of *N*,*N*-dimethylformamide (DMF) solvent. The solution was kept for 24 hours under magnetic stirring to dissolve the P(VDF-TrFE) powders completely. Subsequently, different amounts of g-C_3N_4 nano-powders were added in the resultant solution which was kept at 60 °C for 24 hours. The thick films of P(VDF-TrFE)/g-C_3N_4 nanocomposites with various contents of g-C_3N_4 (15–50 wt%) were obtained by tape casting on a copper substrate and were dried in an oven at 70 °C. The film thickness was 30–100 μm.

The X-ray diffraction (XRD) patterns of the samples was obtained by Rigaku Smart Lab diffractometer operated at 45 kV and 200 mA using Cu Kα radiation ($\lambda = 0.154$ nm). The analysis on vibrations of molecule bonds in the samples was carried out by a Fourier-transform infrared spectrometer (FT-IR, Nicolet iS50). The microstructures of nanocomposite were analyzed by scanning transmission electron microscopy (STEM, Jeol JEM-2100F), piezoelectric force microscopy (PFM, Asylum MFP-3D Infinity) and scanning electron microscopy (SEM, TESCAN, VEGA3). The thermal analyses on the samples (mass of 20 mg) were performed in a differential scanning calorimetry (DSC, TA Instruments Q200) with a heating or cooling rate of 5 °C min^{-1} from 20 to 180 °C. The samples were coated with silver paste on the bottom and top surfaces as the electrodes for the measurement of temperature-dependent dielectric spectrum, which was performed on an LCR meter (Agilent 4287A). The temperature-dependent polarization–electric field (P–E) loops of the nanocomposite samples was obtained by a ferroelectric test system (TF Analyzer 2000E, aixACCT) at 30 to 65 °C. The frequency of the applied electric field was 10 Hz.

3. Results and discussion

3.1 Characterization

The XRD patterns for P(VDF-TrFE) and P(VDF-TrFE)/g-C_3N_4 are shown in Fig. 1. Two sharp peaks at 18.56° and 19° are

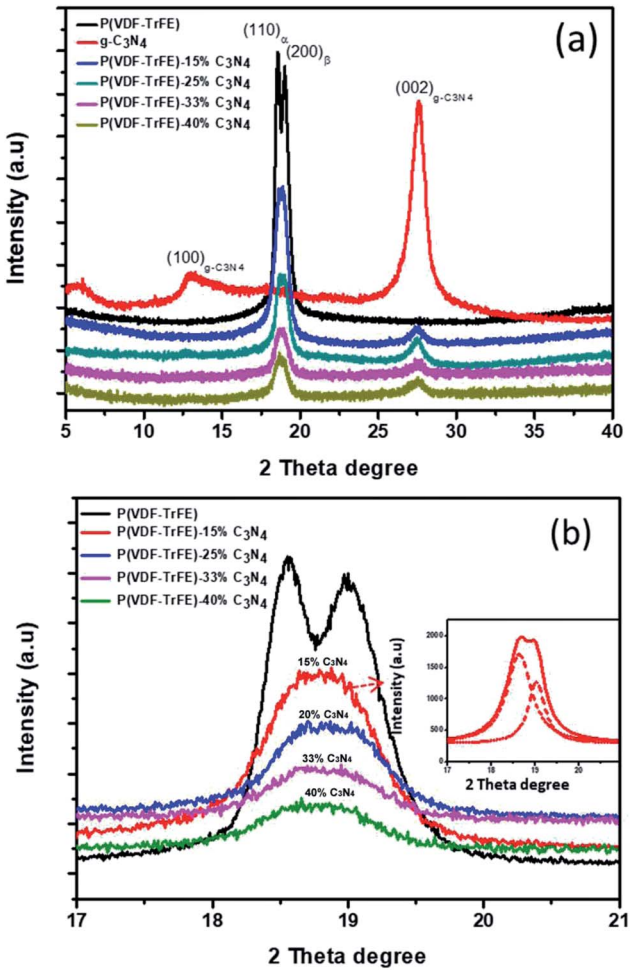

Fig. 1 XRD patterns for g-C_3N_4, P(VDF-TrFE) and P(VDF-TrFE)/g-C_3N_4 nanocomposites (a), and enlarged XRD patterns in the range of 17° to 21° for P(VDF-TrFE) and nanocomposites (b). The inset in (b) shows the deconvolution of the main peak, corresponding to the peaks for α- and β-phase.

associated with the {110} and {200} planes of the α and β phases of P(VDF-TrFE), respectively.[24] The two prominent peaks at 13.04° and 27.51° indexed as (100) and (002) are related with the in-plane structural packing motif units and the interlayer stacking of aromatic of tri-*s*-triazine segments in g-C_3N_4, respectively.[26,27] In the XRD patterns for the nanocomposite, there is a broad peak related with the α-phase and β-phase in P(VDF-TrFE) and the peak intensity decreases gradually with increasing content of g-C_3N_4, suggesting the strong interaction between g-C_3N_4 and the copolymer, as shown in Fig. 1(b). The peak is located at $2\theta = 18.79°$, which is close to that ($2\theta = 19°$) for the β-phase. As shown in Fig. 1(c), the board peak for nanocomposite is analyzed and shows the de-convoluted peaks for α and β phases separately. The peak for β-phase of the nanocomposite can be found to locate at $2\theta = 19°$, which is the same as that of the matrix P(VDF-TrFE).

The surface morphology and microstructure of the P(VDF-TrFE)/g-C_3N_4 nanocomposites are shown in Fig. 2 and 3. Typical PFM signals of surface morphology (height), piezoelectric amplitude and phase for the P(VDF-TrFE)/g-C_3N_4 nanocomposites are shown in Fig. 2(a)–(c), respectively, suggesting the uniform distribution of g-C_3N_4 with sizes of 30–50 nm in the copolymer matrix. The AFM images of g-C_3N_4 and nanocomposites with 25 wt% g-C_3N_4 further reveal that the sizes of g-C_3N_4 nano-powder are as small as 20 nm, as shown in Fig. 3(a and b). The SEM images of copolymer and nanocomposites with 33 wt% g-C_3N_4 indicate the presence of pores in the copolymer (Fig. 3(c)), while the g-C_3N_4 nano-powders are uniformly distributed in the nanocomposites (Fig. 3(d)). Furthermore, the nanocomposite microstructure is investigated by STEM images, which reveals that the sizes of the nano-filler powder g-C_3N_4 are around 20–30 nm, as shown in Fig. 3(e and f), in consistent with those estimated from the PFM images in Fig. 2.

The effects of g-C_3N_4 on the phase transitions in P(VDF-TrFE) are revealed by thermal analyses on the nanocomposite. Fig. 4 shows the DSC results, suggesting that the ferroelectric-to-paraelectric phase transition and melting transition in P(VDF-TrFE) could be significantly affected by the additions of g-C_3N_4. As shown in Fig. 4(a and b), the FE-to-PE phase transition temperature T_c and the melting point T_m of the nanocomposites under heating exhibit maxima near a g-C_3N_4 content of about 25–33 wt%, while the latent heats of phase transitions decrease with increasing content of g-C_3N_4. It can be seen that T_c (at heating) could be increased by almost 2 °C from 61.38 °C to 63.24 °C, as shown in Fig. 4(c), demonstrating that the addition of less than 33 wt% g-C_3N_4 improves the content of β-phase of P(VDF-TrFE) in the nanocomposite.[11,28] On the contrary, the crystallization temperature (T_m at cooling) of P(VDF-TrFE) is found to be increased from 139.21 °C to 145.38 °C as shown in Fig. 4(d), suggesting that the degree of crystallization of the nanocomposite is increased by introducing g-C_3N_4 nano-powders in the P(VDF-TrFE) matrix.[29]

In order to analyze the kinetics of crystallization in the nanocomposites, the samples are first heated to 180 °C well above the melting point and kept for 20 minutes, and then cooled down rapidly with a cooling rate of 80 °C min^{-1} to a crystallization temperature (between 130 °C and 155 °C) close

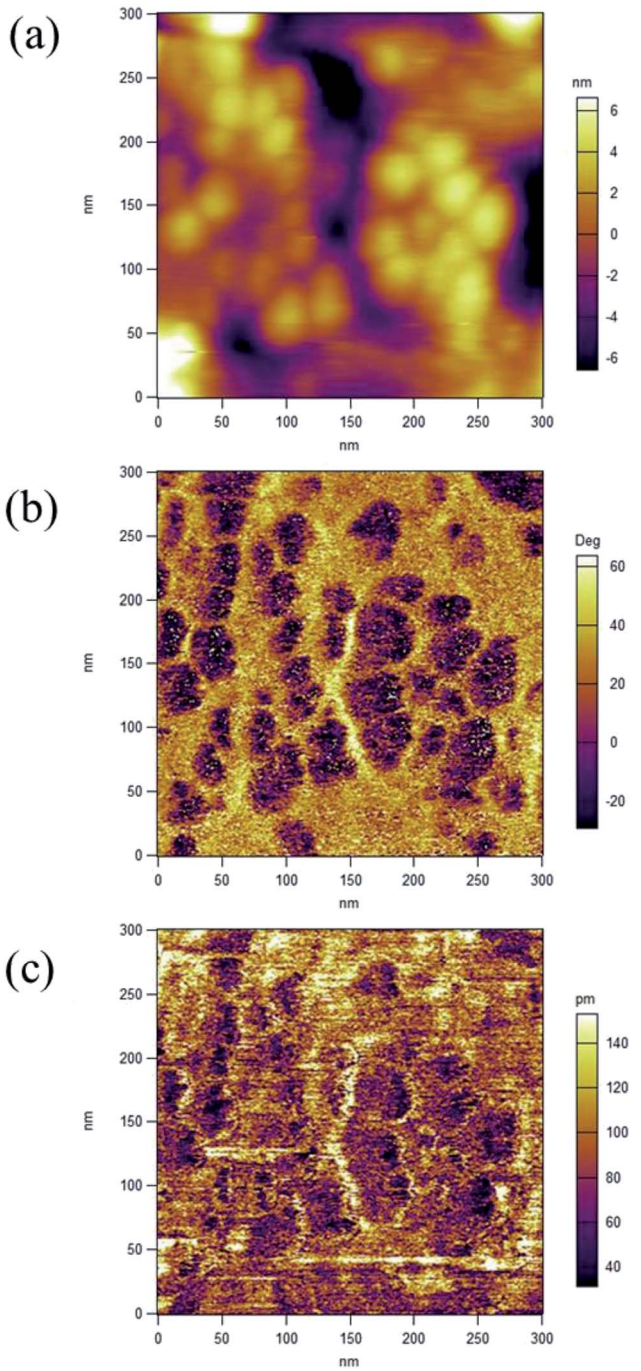

Fig. 2 PFM signals of surface morphology (height) (a), piezoelectric amplitude (b) and phase (c) for P(VDF-TrFE)/g-C_3N_4, respectively.

to the melting point of the samples. The samples are held for 20 minutes at the crystallization temperature. The crystallization fraction $\chi(t)$ of the samples are determined by the following equation[30]

$$\chi(t) = \frac{\int_0^t (\frac{dH}{dt})dt}{\int_0^\infty (\frac{dH}{dt})dt}, \quad (1)$$

where $H(t)$ represents the enthalpy of the crystallization and t represents time elapsed in the crystallization processes. The

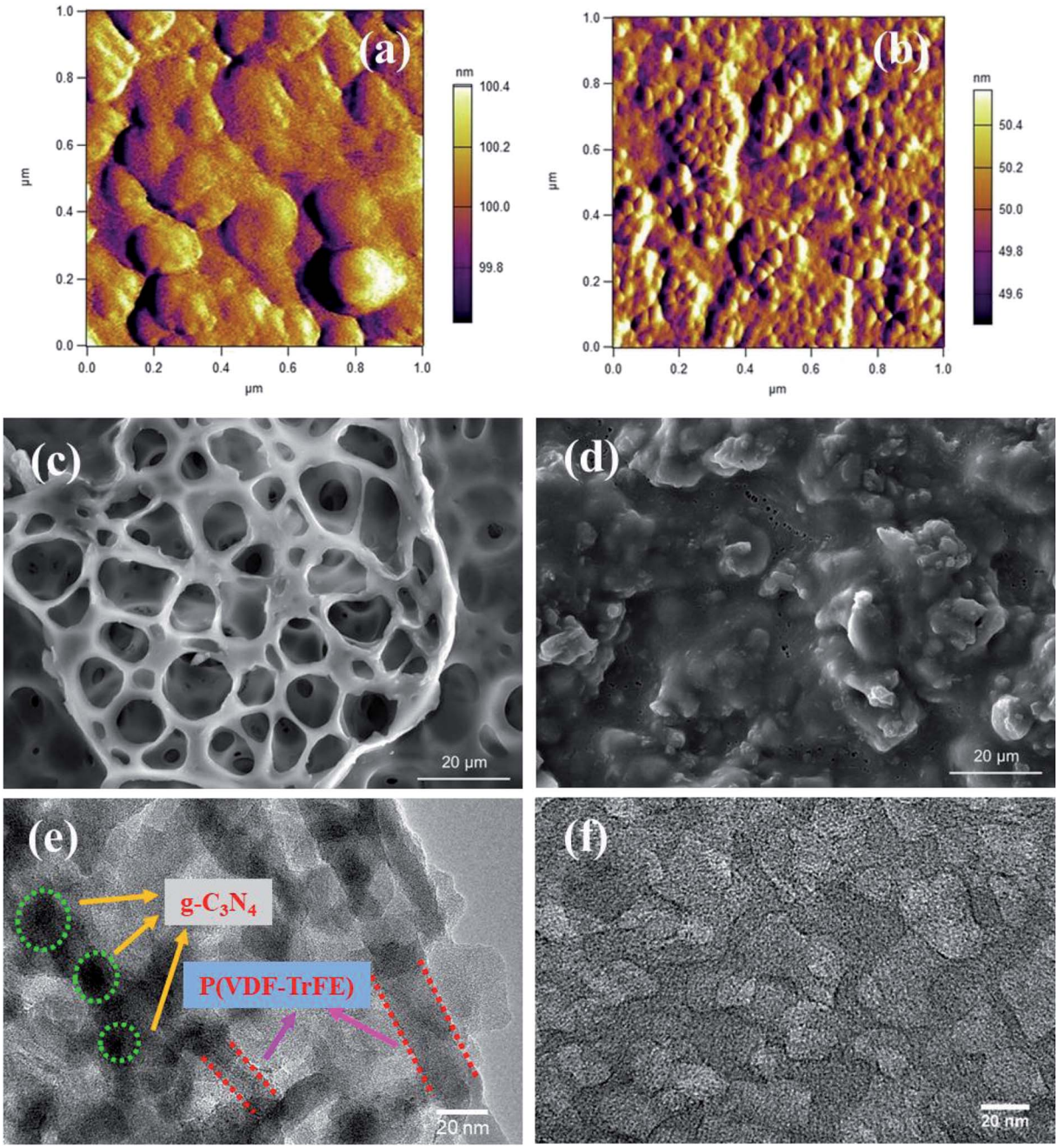

Fig. 3 AFM images of the surface morphology of g-C_3N_4 (a), P(VDF-TrFE)/g-C_3N_4 (25 wt%) (b); and SEM images of P(VDF-TrFE) (c), P(VDF-TrFE)/g-C_3N_4 (33 wt%) (d); and STEM images of P(VDF-TrFE)/g-C_3N_4 nanocomposite at high magnifications (e and f).

completion of the crystallization processes is represented by time limit integration in the denominator in the above equation. By using the value of the crystallization fraction $\chi(t)$ from eqn (1), the feature of crystallization processes is elaborated using Avrami equation,[31–33] as follows:

$$\log[-\ln(1 - x)] = \log Z + n \log t, \quad (2)$$

where Z stands for crystallization rate and n is the Avrami exponent, which determine the nature of crystallization processes.[29,30] Quantitatively, n describes the dimensionality of the space where the crystallization occurs.

Similar procedures are applied to analyze the kinetics of FE-to-PE transition, while the temperature for the isothermal DSC analysis should be below T_c and $\chi(t)$ represents the fraction of polar β phase in P(VDF-TrFE). The isothermal FE-to-PE transition and crystallization processes are characterized by fitting $\chi(t)$ using eqn (2), as shown in Fig. 5. The Avrami exponents n for the nanocomposites with different contents of g-C_3N_4 are listed in Table 1. It can be seen that the values of exponents n for P(VDF-TrFE) and P(VDF-TrFE)/g-C_3N_4 are almost one, revealing that P(VDF-TrFE) and the nanocomposites could exhibit one-dimensional kinetics of phase transitions at T_c and T_m.

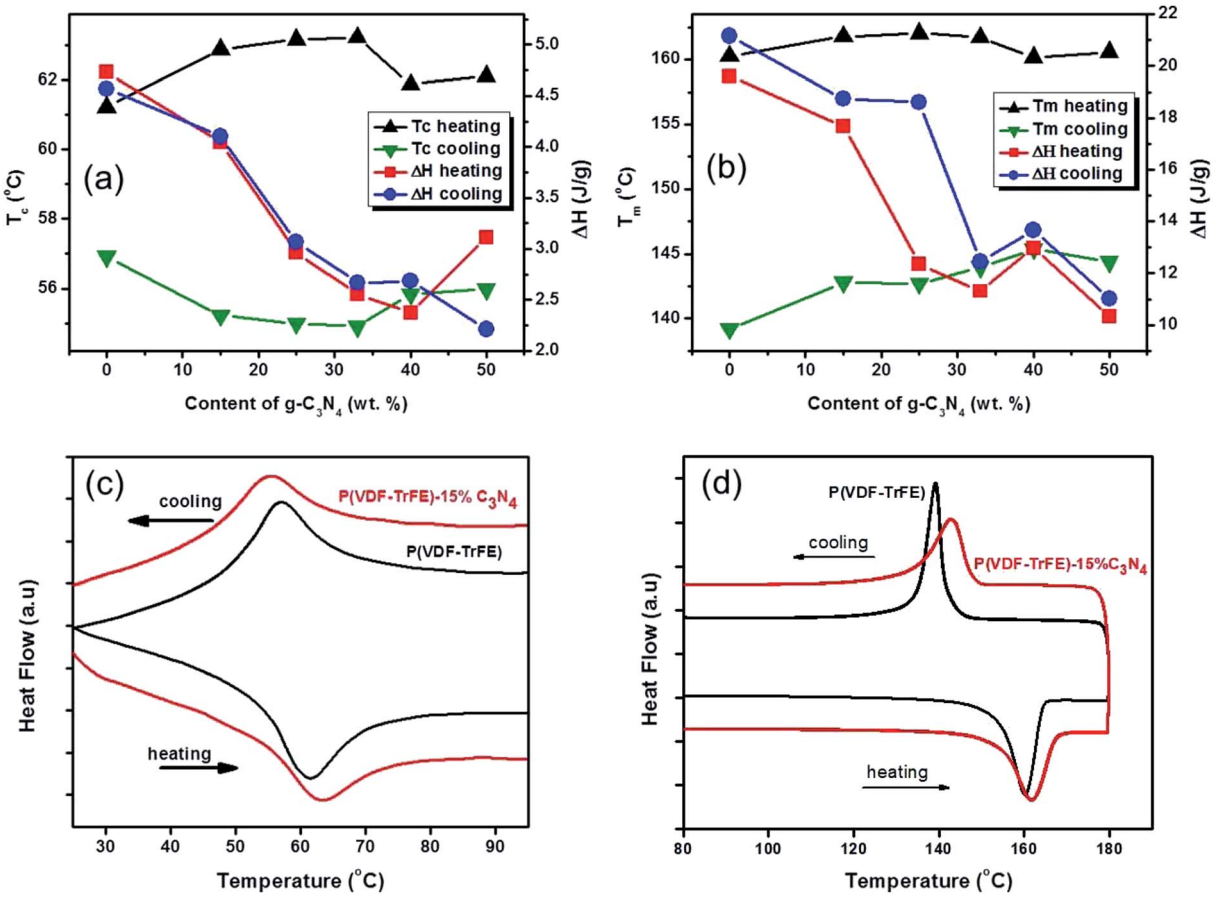

Fig. 4 The FE-to-PE transition temperature T_c (a), and melting or crystallization temperature T_m (b) *vs.* content of g-C_3N_4. Typical DSC heat flow close to T_c (c), and T_m (d), with a temperature varying rate of 5 °C min^{-1}.

The interactions between P(VDF-TrFE) and g-C_3N_4 in the nanocomposites are further investigated by FT-IR spectroscopy. As shown in Fig. 6(a), for g-C_3N_4, the broad peaks centered at 3170 cm^{-1} in the spectra shown are attributed to the N–H stretching vibration mode[34] while the sharp peaks at 1234 cm^{-1}, 1317 cm^{-1} and 1400 cm^{-1} are assigned to the C–N stretching vibration mode.[35] The peak at 804 cm^{-1} corresponds to the breathing mode of triazine system.[36] The three intense bands for β-phase of P(VDF-TrFE) are represented at 847 cm^{-1}, 1285 cm^{-1} and 1400 cm^{-1} in the FT-IR spectra as shown in Fig. 6(b). The absorption band at 1400 cm^{-1} is assigned to the wagging vibration of CH_2 (ref. 37 and 38) and the bands at 847 cm^{-1} and 1287 cm^{-1} are attributed to CF_2 due to the symmetric stretching mode.[39] The band around 2920 cm^{-1} represent symmetric stretching while the band around 2969 cm^{-1} represent asymmetrical stretching of CH_2.[40] For the nanocomposites containing P(VDF-TrFE) and g-C_3N_4, as shown in Fig. 6(b), the β-phase bands for P(VDF-TrFE) are enhanced by adding nano-fillers to the nanocomposite while a sharp peak at about 804 cm^{-1} representing the presence of g-C_3N_4 can be observed. The result reveals that β-phase content of the nanocomposite increases with increasing content of g-C_3N_4. Furthermore, it is believed that the strong interaction exists between C–H molecules of the P(VDF-TrFE) and the NH_2 molecules of g-C_3N_4 because of the formation of NH_3 as reported in ref. 41 and shown in Fig. 6(b) (inset), manifesting itself by the peaks at 3357 cm^{-1} and 3395 cm^{-1} for P(VDF-TrFE)-15% C_3N_4.

The temperature-dependent dielectric constants of the P(VDF-TrFE) and nanocomposite P(VDF-TrFE)/g-C_3N_4 are characterized at different frequencies as shown in Fig. 7. The temperature-dependent permittivity for the pristine P(VDF-TrFE) and nanocomposite P(VDF-TrFE)-15% C_3N_4 at 100 kHz is shown in Fig. 7(a). By introducing the nanofillers, the permittivity of the nanocomposite is significantly increased as compared to the pristine P(VDF-TrFE). The enhanced dielectric permittivity of the nanocomposite could be related with its increased β-phase content as demonstrated by the DSC analysis and FT-IR spectroscopy, resulting in the improved polarization in the nanocomposite as compared with that in the pristine copolymer. The temperature-dependent permittivity of the nanocomposite at the frequencies ranging from 1 kHz to 2 MHz is shown in the Fig. 7(b). The broad peak around 70 °C is attributed to FE-to-PE phase transition and has typically relaxor behaviors characterized by the non-Arrhenius dielectric relaxation.

3.2 Negative electro-caloric effects

The ferroelectric properties of the nanocomposite are further investigated by P–E loop measurements. The hysteresis loops

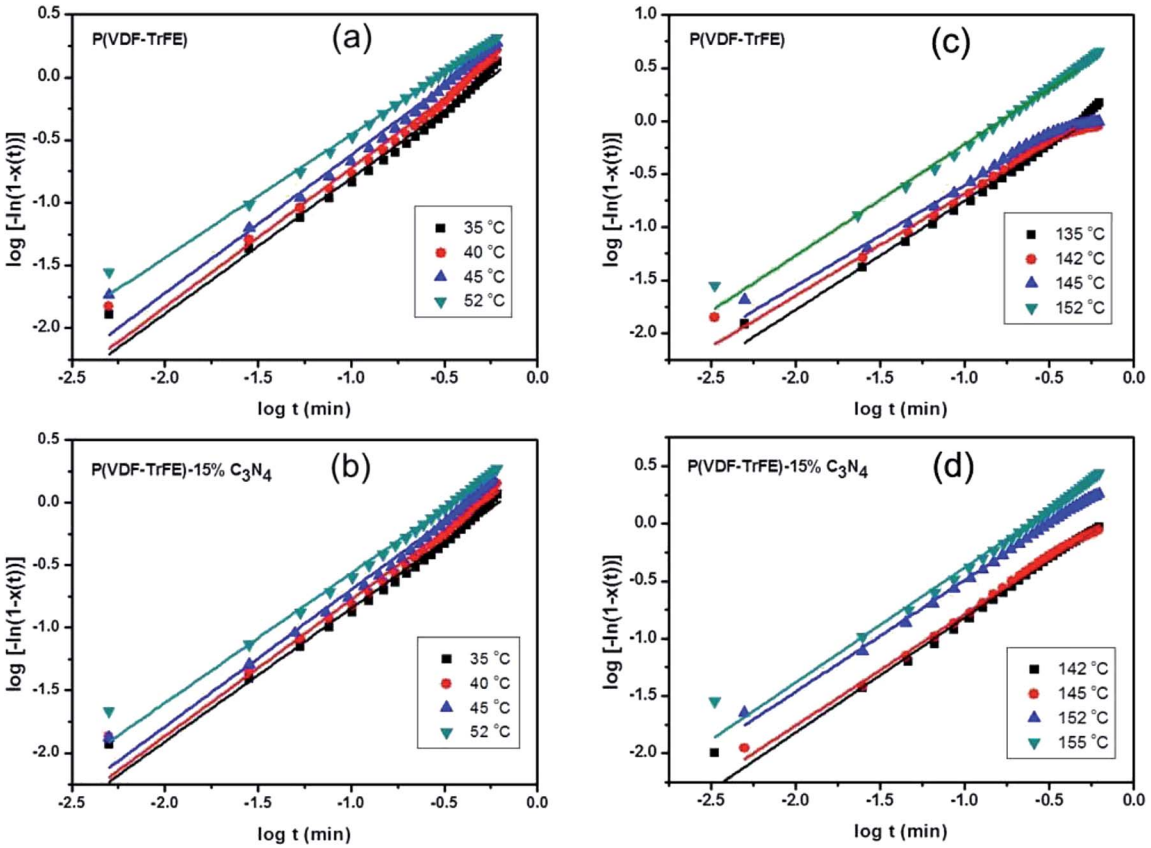

Fig. 5 The fitting of the phase transition fraction $\chi(t)$ close to T_c for P(VDF-TrFE) (a), and P(VDF-TrFE)/15 wt% g-C_3N_4 (b); and the fitting of the crystallization fraction $\chi(t)$ close to T_m for P(VDF-TrFE) (c), and P(VDF-TrFE)/g-C_3N_4(15 wt%) (d), based on the Avrami equation.

form when the varying electric field is applied to the sample and the remnant polarization changes with the temperature. As shown in Fig. 8(a), the P–E loops of P(VDF-TrFE)-15% C_3N_4 nanocomposite show large response to the change of temperature at high electric fields. Adding the nano-powder of g-C_3N_4 into the ferroelectric P(VDF-TrFE) enhances the ferroelectric properties, consistent with that reported for nanocomposite P(VDF-TrFE)/BST.[42] The electrocaloric temperature changes (ΔT) are calculated by thermodynamics Maxwell's equation as

$$\Delta T = -\frac{1}{\rho}\int_{E_1}^{E_2}\frac{T}{C_E}\left(\frac{\partial P}{\partial T}\right)_E \mathrm{d}E, \quad (3)$$

where C_E is the specific heat capacity, ρ is the density and T is the absolute ambient temperature and E_1 and E_2 are the applied electric fields. The values of $(\partial P/\partial T)_E$ are calculated from the fifth-order polynomial fits of the $P_{max}(T)$ data, where P_{max} is the polarization under the maximum applied field. The ECE temperature changes ΔT determined by eqn (3) are shown in Fig. 8(b), indicating a negative ECE in the P(VDF-TrFE)/g-C_3N_4 nanocomposites below T_c. The maximum (absolute) values of negative ECE (5.4 K) are observed at 322 K under 0.45 MV cm^{-1}, for the P(VDF-TrFE)-15% C_3N_4 nanocomposite sample as shown in Fig. 8(b). The strength of negative ECE of P(VDF-TrFE)-15% C_3N_4 (12.0 °C (MV cm^{-1})$^{-1}$) is better than that (~1.24 °C (MV cm^{-1})$^{-1}$) of P(VDF-TrFE) and is even comparable to the conventional ECE value (10–15 °C (MV cm^{-1})$^{-1}$) for terpolymer P(VDF-TrFE-CFE).[43] More importantly, the negative ECE in the P(VDF-TrFE)-15% C_3N_4 nanocomposite is found to be comparable to that of PZT-based thin films under much higher applied fields,[15] suggesting that the P(VDF-TrFE)/g-C_3N_4 nanocomposites could be advantageous over ceramic thin films for ECE applications.

Table 1 The Avrami exponent $n = n_0$ or n_1 for the kinetics of phase transitions close to T_c or T_m, respectively

wt% g-C_3N_4		0	15	25	33	40	50
n_0	40 °C	1.1742	1.1525	1.1366	1.1615	1.2278	1.1751
	45 °C	0.9186	1.0568	0.9766	1.1918	1.2390	1.0102
n_1	142 °C	1.0187	0.9701	1.0518	1.1615	1.1210	1.0365
	148 °C	1.062	0.868	0.9821	1.1918	1.0043	0.9522

3.3 Discussion

As shown in Fig. 7(b), the dielectric relaxation close to the FE-to-PE transition shows typical relaxor characteristics, which could be characterized by the Vogel–Fulcher–Tammann (VFT) relation as follows:[42]

$$f = f_0 e^{-E_a/k_B(T-T_0)}, \quad (4)$$

where f is the test frequency and T is the peak temperature; E_a is the apparent activation energy, f_0 is the attempt frequency and T_0 is the so-call freezing temperature and k_B is Boltzmann

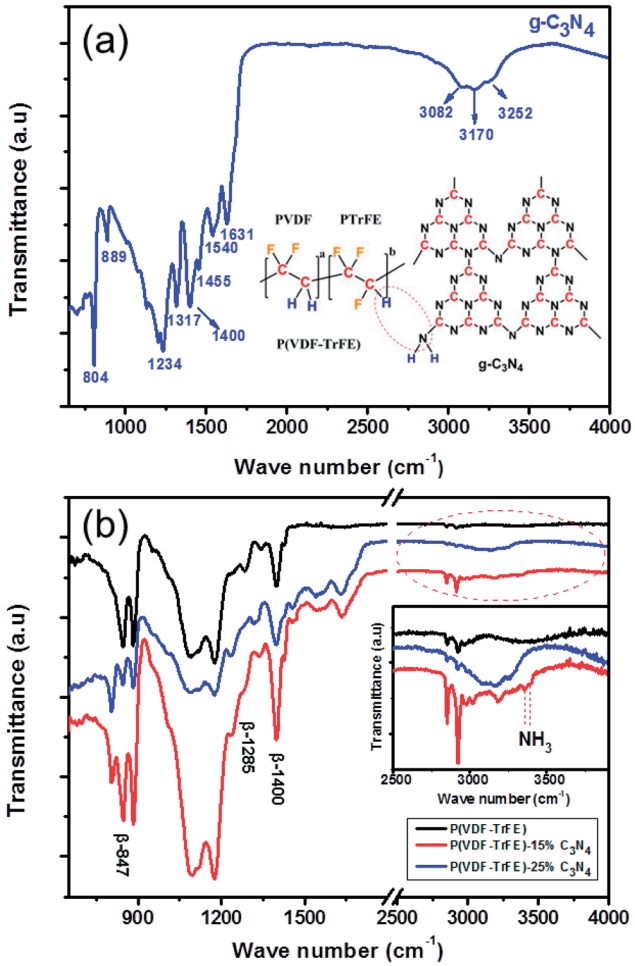

Fig. 6 FT-IR spectra for g-C_3N_4 (a), P(VDF-TrFE) and the nanocomposites with different contents of g-C_3N_4 (b). The inset in (a) and (b) shows the schematic of P(VDF-TrFE)/g-C_3N_4, and the zoom-in view of (b), respectively.

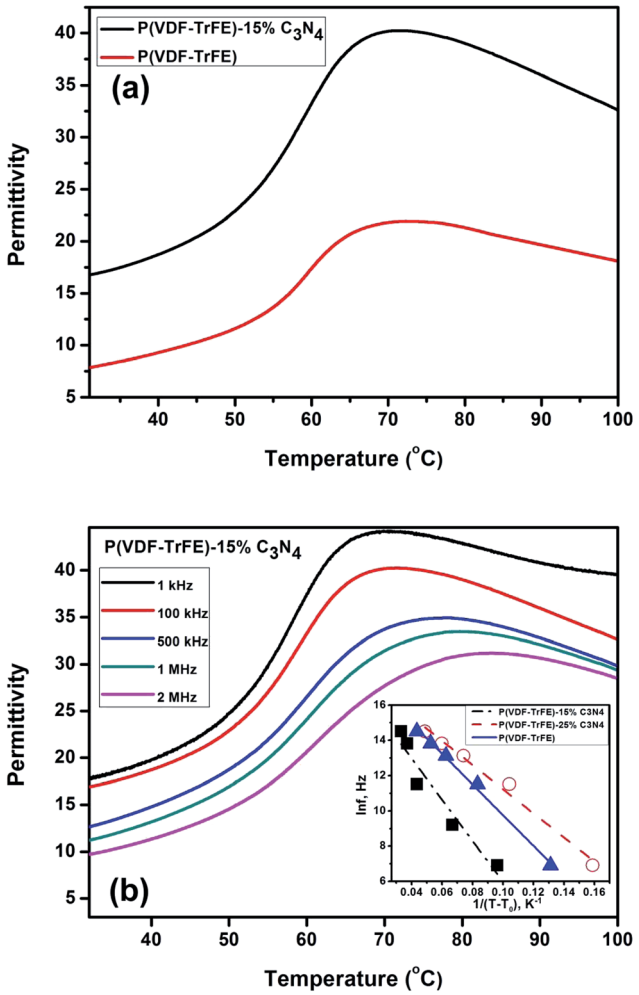

Fig. 7 (a) The temperature-dependent permittivity of P(VDF-TrFE) and the P(VDF-TrFE)-15% C_3N_4 nanocomposites at 100 kHz (a); (b) the dielectric relaxation of P(VDF-TrFE)-15% C_3N_4 nanocomposite; the inset shows the VFT plots.

constant. The activation energy of the nanocomposites is calculated by using eqn (4). The linear fitting of ln f *versus* $1/(T - T_0)$ is shown in Fig. 7(b) (inset) for copolymer and nanocomposites. The apparent activation energy $E_a = 0.01$ eV ($T_0 = 60$ °C) and $E_a = 0.0058$ eV ($T_0 = 60$ °C) are determined for the nanocomposites with 15 wt% and 25 wt% g-C_3N_4, respectively. While for pure P(VDF-TrFE), $E_a = 0.0075$ eV with $T_0 = 60$ °C is recorded. It could be found that T_0 is very close to the Curie temperature T_c shown in Fig. 4(a).

It is worth noting that eqn (4) in the description of dielectric relaxation of the nanocomposite is derived from Kauzmann theory for glassy solids. The entropy S of a glassy solid is described as:[44]

$$S = S_0 e^{-E_a/k_B(T-T_0)}, \quad (5)$$

where S_0 is a pre-exponential factor, and T_0 is defined as a Kauzmann temperature at which the entropy becomes zero. The fact that the dielectric relaxation is well fitted with eqn (4) implies that the nanocomposites at the FE state possess a glassy polar domain structure, which could explain the negative ECE below T_0, as shown in Fig. 8(b). Based on the Kauzmann theory, the configurational entropy of the FE states above T_0 is nonzero, manifesting itself to be increased or decreased under the removal or application of an electric field, respectively, *i.e.*, a conventional ECE. Below T_0, on the contrary, the configurational entropy could be zero according to eqn (5). Therefore the entropy of the nanocomposite has to be increased under the application of an electric field, which is a typical behavior of negative ECE as described by the thermodynamics Maxwell's relation $((\partial S/\partial E)|_T = (\partial P/\partial T)|_E > 0)$ and eqn (3).

More importantly, the Kauzmann theory for negative ECE can well explain why the maximum (absolute) values of negative ECE for the P(VDF-TrFE)-15% C_3N_4 nanocomposite is the largest. Since the negative ECE in the nanocomposites could be related with their glassy states of the polar domains, based on eqn (4), the activation energy E_a that measures the energy barrier for the freezing of glassy polar domain structures with zero entropy S, can be used to measure the strength of negative ECE. For the nanocomposite with a larger E_a, the activation of

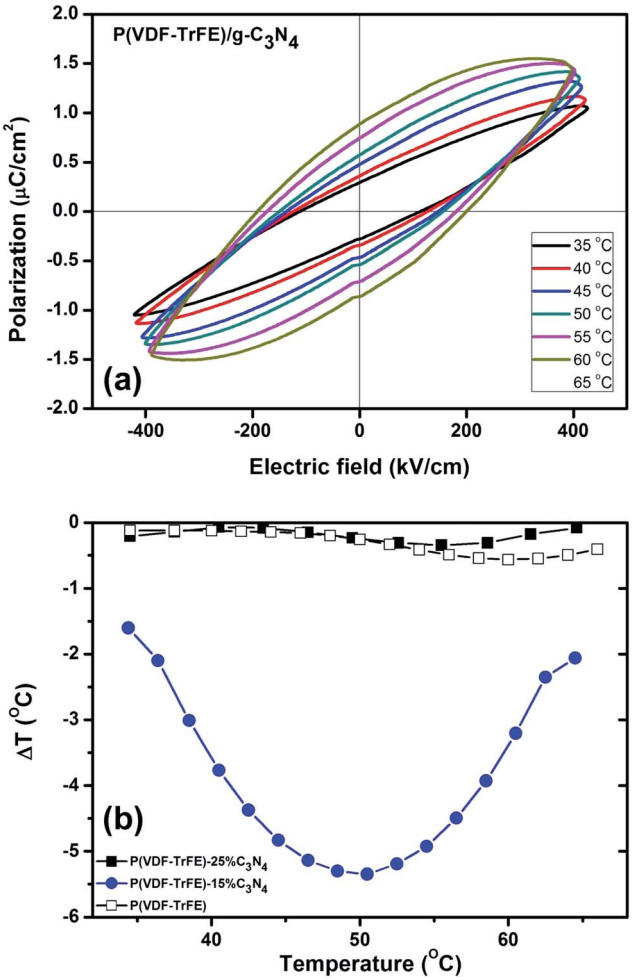

Fig. 8 (a) Temperature-dependent P–E loops of P(VDF-TrFE)-15% C_3N_4 nanocomposite at different applied electric fields (320–400 kV cm^{-1}). (b) The negative ECE temperature change ΔT *versus* T for copolymer and the nanocomposites P(VDF-TrFE)/g-C_3N_4 under an electric field of 450 kV cm^{-1}.

its frozen glassy polar state ($S = 0$) by the applied electric fields could result in a higher entropy change. As a consequence, the negative ECE as measured by the absolute value of ECE temperature change, could increase with increasing E_a that measures the relaxation process of glassy polar domain structures. As shown in Fig. 7(b) (inset), the P(VDF-TrFE)-15% C_3N_4 nanocomposite has the largest E_a as compared with that of P(VDF-TrFE)-25% C_3N_4 or the pristine copolymer. Hence, the P(VDF-TrFE)-15% C_3N_4 nanocomposite has the largest negative ECE.

4. Conclusions

Nanocomposites containing P(VDF-TrFE) and g-C_3N_4 are prepared to improve the dielectric and ferroelectric properties of P(VDF-TrFE). The thermal analyses on the nanocomposites reveal that the degree of crystallization of P(VDF-TrFE) is enhanced by the addition of g-C_3N_4. Particularly, when the content of g-C_3N_4 is less than 33 wt%, the content of polar β phase in P(VDF-TrFE) increases with increasing content of g-C_3N_4 in the nanocomposites. The effects of g-C_3N_4 on the ferroelectric-to-paraelectric phase transition and the crystallization of P(VDF-TrFE) are attributed to the strong interaction between the NH_2 groups in g-C_3N_4 and the CH groups in P(VDF-TrFE), which is revealed by the FT-IR spectroscopy. The negative ECE of nanocomposites can be well described by Kauzmann theory, and the absolute value of ECE temperature change of the nanocomposite is found to be maximized with 15 wt% addition of g-C_3N_4. The results suggest that the addition of g-C_3N_4 in the ferroelectric copolymer is an effective approach in improving its dielectric, ferroelectric and ECE properties.

Conflicts of interest

There are no conflicts to declare.

Acknowledgements

This work was supported by a grant from the Hong Kong Polytechnic University (No. G-YBW4), and National Key R&D Program of China (Grant No. 2016YFC1402504).

References

1 A. Navid, C. S. Lynch and L. Pilon, *Smart Mater. Struct.*, 2010, **19**, 1–13.
2 N. Neumann, R. Köhler and G. Hofmann, *Ferroelectrics*, 1995, **171**, 225–238.
3 S. A. Pullano, I. Mahbub, S. K. Islam and A. S. Fiorillo, *Sensors*, 2017, **17**, 1–13.
4 A. Pecora, L. Maiolo, F. Maita and A. Minotti, *Sens. Actuators, A*, 2012, **185**, 39–43.
5 V. F. Cardoso, C. M. Costa, G. Minas and S. Lanceros-Mendez, *Smart Mater. Struct.*, 2012, **21**, 1–8.
6 R. Köhler, N. Neumann and G. Hofmann, *Sens. Actuators, A*, 1994, **45**, 209–218.
7 H. S. Nalwa, *J. Macromol. Sci.*, 1991, **31**, 341–432.
8 P. Martins, A. C. Lopes and S. Lanceros-Mendez, *Prog. Polym. Sci.*, 2014, **39**, 683–706.
9 M. Li, H. J. Wondergem, M. J. Spijkman, K. Asadi, I. Katsouras, P. W. M. Blom and D. M. DeLeeuw, *Nat. Mater.*, 2013, **12**, 433–438.
10 A. Aliane, M. Benwadih, B. Bouthinon, R. Coppard, F. D. Santos and A. Daami, *Org. Electron.*, 2015, **25**, 92–98.
11 U. Valiyaneerilakkal, A. Singh, C. K. Subash, S. M. Abbas and S. Varghese, *Polym. Compos.*, 2015, **38**, 1655–1661.
12 S. Fujisaki and H. I. Fujisaki, *Appl. Phys. Lett.*, 2007, **90**, 1–3.
13 P. Kobeko and I. Kurchatov, *Z. Phys.*, 1930, **66**, 192–205.
14 Z. Jiang, G. P. Zheng and S. Ullah, *Ceram. Int.*, 2018, **45**, 2876–2880.
15 W. Geng, Y. Liu, X. Meng, L. Bellaiche, J. F. Scott, B. Dkhil and A. Jiang, *Adv. Mater.*, 2015, **27**, 3165–3169.
16 Z. Dang, H. Wang, H. Xu and H. Wang, *Appl. Phys. Lett.*, 2006, **89**, 1–3.
17 D. Gersappe, *Phys. Rev. Lett.*, 2002, **89**, 1–4.

18 G. C. Psarras, K. G. Gatos, P. K. Karahaliou, S. N. Georga and C. A. Krontiras, *eXPRESS Polym. Lett.*, 2007, **1**, 837–845.
19 X. Z. Chen, X. Li, X. S. Qian, M. Lin, S. Wu, Q. D. Shen and Q. M. Zhang, *Polymer*, 2013, **54**, 5299–5302.
20 G. Zhang, Q. Li, H. Gu, S. Jiang, K. Han, M. R. Gadinski, M. A. Haque, Q. Zhang and Q. Wang, *Adv. Mater.*, 2015, **27**, 1450–1454.
21 W. Wu, X. Huang, S. Li, P. Jiang and T. Toshikatsu, *J. Phys. Chem.*, 2012, **116**, 24887–24895.
22 Q. Wang and L. Zhu, *J. Polym. Sci., Part B: Polym. Phys.*, 2011, **49**, 1421–1429.
23 S. Adireddy, V. S. Puli, T. J. Lou and D. B. Chrisey, *J. Sol-Gel Sci. Technol.*, 2015, **73**, 641–646.
24 J.-H. Lee, K. Y. Lee, B. Kumar, N. T. Tien, N.-E. Lee and S.-W. Kim, *Energy Environ. Sci.*, 2013, **6**, 169–175.
25 B. Yu and B. Wang, *Composites, Part B*, 2017, **79**, 277–284.
26 L. Qiu, *J. Mater. Chem. A*, 2013, **1**, 3008–3015.
27 B. Yuan, Z. Chu, G. Li, Z. Jiang, T. Hu, Q. Wang and C. Wang, *J. Mater. Chem. C*, 2014, **2**, 8212–8215.
28 T. Feng, D. Xie, Y. Zang, X. Wu, T. Ren and W. Pan, *Integr. Ferroelectr.*, 2013, **141**, 187–194.
29 G. Z. Papageorgiou, D. S. Achilias, D. N. Bikiaris and G. P. Karayannidis, *Thermochim. Acta*, 2004, **427**, 117–128.
30 V. Sencadas, C. M. Costa and J. L. Go, *J. Mater. Sci.*, 2010, **45**, 1328–1335.
31 M. Avrami, *J. Chem. Phys.*, 1939, **7**, 1103–1112.
32 M. Avrami, *J. Chem. Phys.*, 1940, **8**, 212–224.
33 M. Avrami, *J. Chem. Phys.*, 1941, **9**, 177–184.
34 N. M. Reynolds, K. J. Kim, C. Chang and S. L. Hsu, *Macromolecules*, 1989, **21**, 1092–1100.
35 T. Giannakopoulou and N. Todorova, *Appl. Surf. Sci.*, 2015, **358**, 278–286.
36 X. Li, M. Li, J. Yang, X. Li, T. Hu and J. Wang, *J. Phys. Chem. Solids*, 2014, **75**, 441–446.
37 Z. Y. Jiang, G. P. Zheng, Z. Han, Y. Z. Liu and J. H. Yang, *J. Appl. Phys.*, 2014, **115**, 204101–204106.
38 R. I. Mahdi, W. C. Gan and W. Majid, *Sensors*, 2014, **14**, 19115–19127.
39 M. Kobayashi, K. Tashiro and H. Tadokoro, *Macromolecules*, 1974, **8**, 158–171.
40 R. M. Habibur, U. Yaqoob, S. Muhammad, A. S. M. I. Uddin and H. C. Kim, *Mater. Chem. Phys.*, 2018, **215**, 46–55.
41 V. Vinogrado, F. Duvernay, G. Danger, P. Theulé and T. Chiavassa, *Astron. Astrophys.*, 2011, **530**, 1–7.
42 Z. Y. Jiang, X. C. Zheng and G. P. Zheng, *RSC Adv.*, 2015, **5**, 61946–61954.
43 D. Guo, J. Gao, Y.-J. Yu, S. Santhanam, G. K. Feder, A. J. H. McGaughey and S. C. Yao, *Appl. Phys. Lett.*, 2014, **105**, 1–6.
44 W. Kauzmann, *Chem. Rev.*, 1948, **43**, 219–256.